CHAPTER–5

Transmetalation Reaction and Adsorption Properties of Coordination Polymers of Bis(4-pyridyl)-phenylene-diamide

Transmetalation Reaction and Adsorption Properties of Coordination Polymers of Bis(4-pyridyl)-phenylene-diamide

5.1 Introduction

Crystal engineering of metal-organic frameworks (MOF) or coordination polymers (CPs) has shown multidimensional applications in the areas of gas storage,[1] catalysis,[2] magnetism,[3] luminescence materials,[4] electrical conductivity,[5] biological applications[6] and so on. Design strategies require the synthesis of ligands or linkers which can enable the extension of CPs or MOFs into higher dimensionality not only by utilizing coordinate bond interactions but also by involving non-covalent interactions such as hydrogen bond interactions.[7] Overall geometry of a CP or MOF depends on many factors which include solvent, temperature, pH etc.[8] Design of CPs using ligands equipped with hydrogen bond functionalities can lead to the formation of networks which can recognize counter anions and various guest molecules via hydrogen bond interactions. One of the well-known hydrogen bond functionality is the amide group[9] which has been utilized widely in anion recognition[10] and separation. Pyridyl based exo-bidentate ligands (Scheme 5.1), where pyridyl groups are separated by amide moieties and an alkylene/arylene spacer, involve a combination of amide functionality for hydrogen bond interactions and pyridyl groups for coordination bond interactions.

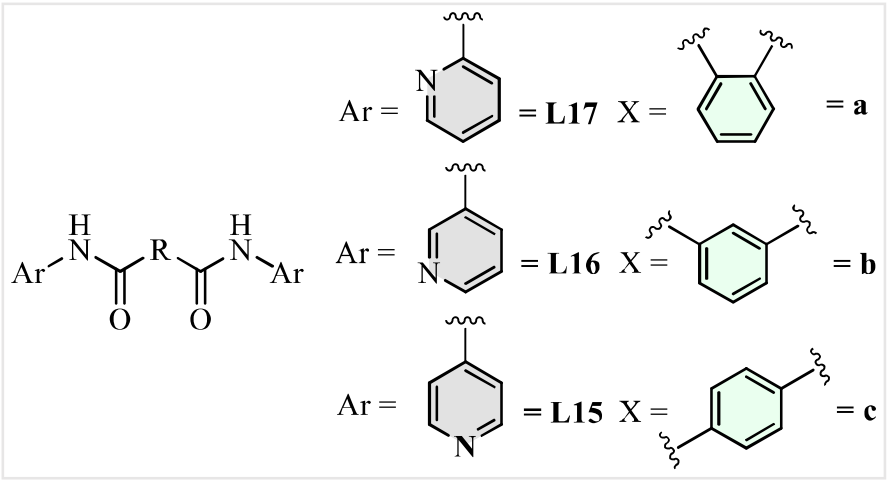

Scheme 5.1: Pyridyl based exo-bidentate ligands equipped with groups for coordinate bond as well as hydrogen bond interactions

Dastidar and co-workers have synthesized metal-organic frameworks (MOFs) with **L16b** and **L15b** wherein they analyzed the structural diversities of the MOFs resulting due to the positional isomerism of ligands and also performed counter anion exchange studies of the MOFs.[11] They have also reported a 2D corrugated sheet[12] with **L16b**, metallogels[13] with **L16b** and **L16c**, and a borromean weave CP[14] with **L16c**. Among various important applications, they have shown the isolation of fluoride ion using a 3D non-interpenetrated CP

of **L16b** and **L16c**.[15] Mukherjee and co-workers have explored coordination driven self-assembly by using **L16b**/**L15b** ligands, which resulted in the formation of nanoscopic prism,[16] molecular prism,[17] Pt(II) based metallomacrocycles,[18] Pd(II) based molecular rectangles,[19] octanuclear Pt(II) based tetragonal prism,[20] hexanuclear Pt(II) based nanoscopic cages,[21] Pt(II) based macrocycles[22] and explored their various applications such as sensing of nitroaromatics etc. Gong et al., have prepared CPs using **L15b**, which showed reversible color change by desolvation and solvation.[23] Han et al., have reported CPs by using dicarboxylic acids along with **L15b** and observed the effect of temperature on the conformations of **L15b** in the CPs.[24] Gong et al., have also designed MOF based on mok nets topology where dicarboxylic acid was used as a co-ligand.[25] Further they have exploited the photo-luminescence properties of the CPs from **L15b** and **L15c** along with various dicarboxylic linker.[26] Gong et al., have also synthesized a supercapacitor material by using **L15b** and diacid ligands, wherein, **L15b** formed 1D looped chain with the metal center which is further connected by a diacid linker to form a 3D microporous architecture network.[27] Puddephatt and co-workers have synthesized several palladium lantern[28] type complexes and laminated sheet-like[29] structure of CPs by using **L15b** and **L16b** ligands for application in host-guest chemistry. Biradha and co-workers have synthesized CPs of varied networks and geometries and elaborately studied their assembling via hydrogen bond interactions.[30] They have reported CPs of **L16c** and **L15c** with guest molecules such as benzonitrile,[31] nitrobenzene[32] and also without guest molecules.[33] Luo's group has exploited **L16b**, **L16c** and **L15b** in synthesizing CPs and studied their photo-switching behaviour,[34] xylene isomer sensing,[35] phosphor material[36] and photoluminescence[37]. They have also shown a solvent induced change in network geometry of a CP of **L16b**.[38]

Post-synthetic structural modulation in CPs/MOFs can be triggered by various external stimulus such as ion exchange, thermal effect, solvent effect, light induced, mechanochemical forces and so on. Post-synthetic modification of CPs can be utilized efficiently to tailor made the CPs to get desired properties which may not be possible via direct synthesis.[39] Kim and co-workers have reported single-crystal-to-single-crystal transformation (SC-SC) of a Cd(II) based CP of 5,5,10,10,15,15-Hexaethyltruxene-2,7,12-tricarboxylic acid wherein the Cd(II) centers were replaced by Pb(II) and 98% of the transformation was observed within 2 h.[40] They have also synthesized Co/Ni/Cu frameworks via metal metathesis of Mn(II) MOF of 5,5,10,10,15,15-Hexamethyltruxene-2,7,12-tricarboxylic acid and observed metal specific properties related to hydrogen adsorption and magnetization.[41] Tian et al., have prepared an anionic MOF using tetrakis[4-(carboxyphenyl)oxamethyl]methane and observed SC-SC

transformation leading to the selectively capture Co^{2+} and Ni^{2+} among various transition metals.[42] Bharadwaj and co-workers have reported SC-SC transformation wherein Zn(II) in the MOF of 2′-amino-[1,1′:3′,1″terphenyl]-3,3″,5,5″-tetracarboxylic acid was replaced by Cu(II) and observed an enhanced CO_2 adsorption property in the Cu(II) MOF than the pre-synthesized MOF.[43] Zhou and co-workers have post synthetically performed the synthesis of MOF of earlier transition metals such as Cr (II) and Fe (II) where a step by step SC-SC transformation of Mg(II) MOF of 2′,3″,5″,6′-tetramethyl-[1,1′:4′,1″:4″,1‴-quaterphenyl]-3,3‴,5,5‴-tetracarboxylic acid resulted in the corresponding Cr(II) and Fe(II) MOFs.[44] Tomar and co-workers have shown an improved catalytic activity of a CP of Zn(II) using 5-(benzylamino)isophthalic acid after post-synthetic replacement of Zn(II) to Cu(II).[45] Das and co-workers have reported a quantitative transmetalation of Zn(II) to Cu(II) by employing Bis(pyrazolyl)pyridine carboxylate ligand.[46] Our group has previously reported a transmetalation reaction in a Cd(II) CP of N^1,N^6-di(pyridin3-yl)adipamide, where Cd(II) centers were completely replaced by Cu(II) ions without altering the geometry of the network.[47]

Dye effluents are the result of various industrial sources like paper, rubber, textile, printing, cosmetics, leather and plastics.[48] Many such non-biodegradable dyes are carcinogenic and also have harmful effects on the aquatic environment. Several photocatalysts has been used in dye degradation such as graphene based photocatalyst[49], metal oxide photocatalyst[50] and CPs/MOFs[51] based photocatalyst. Zhao's group has developed a graphene based photocatalyst with 3D porous carbon nanotubes and observed its effectiveness in degrading rhodamine B (RB) under UV light irradiation.[52] A TiO_2 supported graphene composite is reported by Han's group which acted as a photocatalyst for methylene blue (MB) degradation under UV light.[53] Xu's group has been involved in developing efficient photocatalysts for degrading RB using graphene modification through tuning[54] and doping[55]. An elaborate review by Xu's group showcased the developments and drawbacks of photocatalyst.[56]

Last two decades have seen a considerable rise in the research involving the use of MOFs/CPs in purification of water using photocatalytic technology.[57] Presence of porosity in MOFs/CPs is one of the most advantageous property which makes them a suitable candidate for photocatalysis. In photocatalytic degradation of dyes, previous studies mainly involved the usage of 60% of UV light and 30% of visible light. Now researchers are more focused in utilizing 10% of solar light as natural energy sources.[58] Proper selection of metal ions along with N and O containing conjugated ligands are required to tailor made CPs/MOFs, which can

result in enhanced photocatalytic efficiency. Porosity in CPs/MOFs will be effective in providing large surface area to incorporate O_2/OH radical for degrading the dye. There are many reports on photocatalysis involving Cu(II), Zn(II) and Cd(II) MOFs using ligands such as imidazole[59], pyrazole[60] etc. Mahata et al., have synthesized Ni(II) and Co(II) CPs of 4,4′-oxybis(benzoate) and 4,4′-bipyridine ligands wherein the CPs were observed to degrade the Rhodamine B (RB), Methylene Blue (MB) and Remazol Brilliant Blue R (RBBR).[61] Wang's group has synthesized a 2D Zn(II)-MOF based on 4-(pyridyli-4-yl) phthalic acid which showed photocatalysis in degrading RB and methyl orange (MO) up to 98.5% and 83.8% efficiency respectively in absence of any photosensitizer.[62] Yang's group has reported efficient photocatalysis of MB, RB and MO by using Cu-triazolate MOF.[63] One of the major challenges in using MOFs/CPs as photocatalyst is its stability in aqueous medium. Bedia and co-workers have done an extensive review on the challenges related to using MOFs/CPs as photocatalyst; which include stability of MOFs/CPs in aqueous medium under visible light, loading amount required for catalysis, recyclability and rate of degradation of dyes.[64] MIL-53 Fe(III) (MIL: Material Institute Lavoisier) is one of the MOF examples which was studied as photocatalyst for dye degradation in water system.[65] It was also reported that other MIL MOFs, UiO-66 (University of Oslo) and ZIFs (Zeolitic imidazolate frameworks) series acted as efficient water-stable photocatalyst. A recent review by Qi Wang and Shengqian Ma showed an extensive coverage on the developments of MOF based visible light photocatalyst.[66]

High-temperature sustainability, tunable porosity, and dimensionality associated with CPs/MOFs make them favorable candidates in the applications involved in charge transport.[67] Kitagawa and co-workers have reported the encapsulation of proton carrier imidazole molecule into a porous CP and observed an increase in the conductivity to 2.2×10^{-5} S cm^{-1} at 120 °C.[68] Fuma et al., have reported an increase in conductivity to 1.4×10^{-3} S cm^{-1} due to the rehydration of water molecules in the interstitial site of a CP.[69] You et al., have synthesized an MOF, **NH_4Br@HKUST-1** by soaking **HKUST-1**, which is a MOF built from Cu-paddle wheel nodes with 1,3,5-benzene-tricarboxylate struts, in a saturated ethanolic solution of NH_4Br and observed an increase in conductivity by three/four orders of magnitude in **NH_4Br@HKUST-1** than that in **HKUST-1**.[70] H. Kitagawa's group has synthesized a porous coordination polymer by introducing electron donors and acceptors as building units, which showed high electrical conductivity (6×10^{-4} S cm^{-1}).[71] Himoto et al., have synthesized several semiconducting CP using mixed valance metal ions and dithiocarbamate ligands.[72] Banerjee

and co-workers have reported first proton conducting CP based on polyoxometalate and achieved a conductivity of 2.2×10^{-5} S cm^{-1}.[73]

In this chapter, we have used N^1,N^3-di(pyridine-4- yl)isophthalamide, **L15b** (Bis(4-pyridyl)-phenylene-diamide), to synthesize a Co(II) based coordination polymer, **CP1**. Transmetalation reaction of **CP1** with Cu(II) resulted in SC-SC transformation to form **CP2**. The ligand **L15b** has a 1,3-disubstituted aromatic group in the spacer along with two amide groups (Scheme 5.1). Presence of 1,3-disubstituted aromatic moiety has resulted in 'V' shaped geometry to the ligand **L15b** while the amide groups being important hydrogen bond functionalities, will be actively involved in diverse non-covalent interactions leading to possibilities of varied geometries and properties of CPs. An exo bidentate 'V' shaped rigid ligand **L15b** is used in the current study specifically to ascertain the possibility of generating porous networks. **CP1** and **CP2** showed some marked property difference due to the effect of replacing Co(II) with Cu(II).

5.2 Experimental

5.2.1 General

^{1}H and ^{13}C Nuclear Magnetic Resonance spectra were recorded on a 400 MHz spectrophotometer (Bruker). IR spectra were obtained from Shimadzu model-00247 IRAffinity-1S. Thermogravimetric analysis performed by using Perkin Elmer TGA4000 with the flowing rate of N_2 is 10 °C/min. PXRD were recorded with a Rigaku miniflex ll, λ =1.54 Å, Cu Kα. The elemental analysis (C, H, N, S) were performed by using Vario elemental analyzer. UV-Visible Spectra were recorded using Jasco V-650 spectrophotometer. Atomic absorption spectra were measured using AA-7000, Shimadzu. EDX analysis was done by Leica Ultra Microtome EMUC7, Apreo LoVac model with Aztec Standard EDS system-resolution 127 eV on Mn-Kα. The impedance was measured by computer interfaced HIOKI impedance analyser model IM3570. Isophthaloyl chloride and 4-aminopyridine are purchased from Sigma Aldrich. All others chemical like DMF, KSCN, $Cu(NO_3)_2.6H_2O$, $Co(NO_3)_2.6H_2O$, Methylene blue, Malachite green, Rhodamine B, Methyl orange and solvents are purchased from reagent grade and used further without purification.

5.2.2 Single crystal X-ray diffraction (XRD) studies

The single crystal XRD analysis of **CP1** and **CP2** was done at IISER Mohali, Punjab, using a Bruker Kappa APEX II diffractometer equipped with a CCD detector and sealed tube monochromated MoKα radiation. The structures were solved by using the program APEX2.

By using the program SAINT for the integration of the data, reflection profiles were fitted, and values of F^2 and $\sigma(F^2)$ for each reflection were obtained. Data were also corrected for Lorentz and polarization effects. The subroutine XPREP was used for the processing of data that included determination of space group, application of an absorption correction (SADABS), merging of data, and generation of files necessary for solution and refinement.[74] The structure was solved by direct methods and refined by least square methods on F^2 using SHELX-97.[75] Non-hydrogen atoms were refined anisotropically and hydrogen atoms were fixed at calculated positions and refined using a riding model. The single crystal structural information was deposited into the Cambridge Crystallographic Data Centre (CCDC numbers for **CP1** and **CP2** are 1981911 and 1981912, respectively).

5.2.3 Synthesis of *N*^{1},*N*^{3}-di(pyridine-4-yl)isophthalamide (L15b)

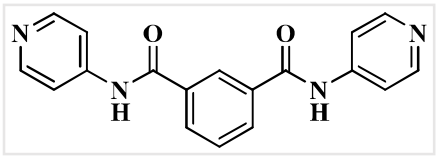

L15b was synthesized by the usual method where isophthaloyl chloride (5 mmol) and 4-aminopyridine (10 mmol) were taken separately in 15 mL of THF solution and kept at 0 °C. Isophthaloyl chloride was added dropwise into 4-aminopyridine which was followed by the addition of trimethylamine (15 mmol). The white precipitate was filtered and washed with 50% ethanol-water mixture. Yield: 70%; Melting point: (215-219) °C; Selected FTIR peaks (KBr, cm^{-1}): 1681(s), 1604 (s), 1504 (s), 1319 (m), 1249 (s), 1188 (m), 1134 (m), 825 (s), 717 (m) (Figure A-104). ^{1}H NMR (400 MHz, DMSO-d6) δ ppm: 11.22 (s, 1H), 11.06 (s, 1H), 8.64 – 8.55 (m, 5H), 8.24 (dd, J = 7.8, 1.8 Hz, 2H), 8.03 (d, J = 5.5 Hz, 2H), 7.95 (d, J = 5.6 Hz, 2H), 7.72 (t, J = 7.8 Hz, 1H) (Figure A-105). ^{13}C NMR (100 MHz, DMSO-d_6) δ 167.12, 167.03, 166.50, 160.32, 140.21, 129.56, 114.95, 109.22 (Figure A-106).

5.2.4 Synthesis of CP1, {[$Co_{0.5}$ (L15b)(NCS)]·1.5(DMF)}$_n$

An ethanolic solution (10 mL) of $Co(NO_3)_2.6H_2O$ (0.0145 g, 0.05 mmol) was layered slowly over a mixture of **L15b** (0.0318 g, 0.1 mmol) and KSCN (0.0392 g, 0.4 mmol) in 45 mL DMF. Pink coloured crystals were obtained after 4-5 days. Yield: 77%; Selected FTIR peaks (KBr, cm^{-1}): 2075 (vs), 1663 (s), 1598 (s), 1512 (s), 1419 (m), 1327 (m), 1296 (m), 1242 (m), 1203 (m), 1134 (m), 1010 (vs), 840 (m), 786 (m) (Figure A-107a). Anal. calcd for $C_{47}H_{49}CoN_{13}O_7S_2$ (%): C, 54.75; H, 4.79; N, 17.66; S, 6.22; Found (%): C, 51.68; H, 4.35; N, 16.90; S, 5.46 (Figure A-107b). Powder XRD (Figure A-108).

5.2.5 Synthesis of CP2, $\{[Cu(L15b)_2(NCS)_2]\cdot 4(DMF)\}_n$

CP1 crystals were soaked into a 10 mL of DMF solution of $Cu(NO_3)_2.6H_2O$ (0.0120g, 0.05 mmol). The pink color crystals were turned into blue colour crystals within couple of hours; however, the crystals of **CP2** were isolated after 2 days. Yield: 78%; Selected FTIR peaks (KBr, cm^{-1}): 2052 (s), 1689 (vs), 1651 (vs), 1597 (vs), 1512 (s), 1419 (s), 1388 (s), 1327 (s), 1296 (s), 1203 (s), 833 (s), 717 (m) (Figure A-109a). Anal. calcd for $C_{50}H_{56}CuN_{14}O_8S_2$ (%):C, 54.16; H, 5.09; N, 17.69; S, 5.78; Found (%): C, 53.52; H, 3.36; N, 15.09; S, 6.15 (Figure A-109b). Powder XRD (Previous Figure A-108).

5.2.6 Photocatalytic experiment

The photocatalytic reactions were monitored by UV-visible spectrophotometer. **CP1**/**CP2** (20 mg) was taken into 10 mL of 10^{-5} M of a dye solution (Methylene blue (MB), Methyl orange (MO), Malachite green (MG) or Rhodamine B (RB)). The dye solution was kept on a magnetic stirrer under visible light (Light source: 8W CFL light). After specified time intervals, 2 mL aliquots were pipetted out from the dye solution and clear solution was obtained by centrifugation. UV-Visible spectrometer was used to record the absorbance of the dye solution. The following wavelengths were monitored for each dye: MB at 664 nm, MO at 464 nm, MG at 616 nm and RB at 554 nm. A similar experiment was repeated by keeping the reaction mixture of **CP1**/**CP2** and a dye solution under a light source of 256 nm.

5.2.7 Magnetic measurement

The magnetic measurement of **CP1** was performed at IIT Roorkee using MPMS ever cool magnetometer. 1000 oersted magnetic field was applied by varying the temperature from 1.9 K to 400 K.

5.2.8 Thermochromism property

The thermochromism studies on **CP1**/**CP2** were done by heating the crystals to about 120°C, which resulted in **CP1*** and **CP2***. Noticeable colour change was observed after 4-5 hours. The reversibility in thermochromism was monitored by soaking the crystals of **CP1*** and **CP2*** back in DMF solution. Within half an hour, the colour of the crystals changed back to their original colour.

5.2.8.1 CP1*: Selected FTIR peaks (KBr, cm^{-1}): 2361 (w), 2068 (vs), 1686 (w), 1655 (m), 1508 (s), 1420 (m), 1234 (w), 1207 (s), 1096 (m), 1072 (m), 829 (m), 536 (s) (Figure A-110). PXRD (Figure A-111) and TGA (Figure A-112) was recorded.

5.2.8.2 CP2*: Selected FTIR peaks (KBr, cm^{-1}): 2052 (s), 1690 (m), 1651 (s), 1593 (s), 1512 (vs), 1423 (m), 1389 (m), 1327 (m), 1296 (m), 1207 (s), 1099 (m), 829 (m), 540 (vs) (Figure A-113). PXRD (Previous Figure A-111) and TGA (Figure A-114) was recorded.

5.2.9 Iodine adsorption and desorption studies

10 mg of **CP1**/**CP2** were immersed into 3 mL of 10^{-4} M iodine solution in hexane. After 30 minutes time intervals, the absorbance of the solution was measured (Absorbance maxima for I_2 is at 522 nm). This process was continued until the absorbance at 522 nm become zero. After that colourless hexane solution was decanted off and the iodine adsorbed crystals (**I_2@CP1** and **I_2@CP2**) were dried. The iodine adsorbed crystals, **I_2@CP1** and **I_2@CP2**, were soaked into a methanolic solution for the desorption process. After a time, interval of 30 mins., the absorbance was recorded at λ = 359 nm.

5.2.9.1 I_2@CP1: Selected FTIR peaks (KBr, cm^{-1}): 2361 (m), 2068 (s), 1686 (w), 1659 (m), 1589 (vs), 1504 (vs), 1331 (m), 1288 (m), 1234 (w), 1207 (m), 1099 (w), 1014 (m), 829 (m), 536 (vs) (Figure A-115). PXRD (Previous Figure A-116) and TGA (Figure A-117) was recorded.

5.2.9.2 I_2@CP2: Selected FTIR peaks (KBr, cm^{-1}): 2361 (w), 2056 (m), 1690 (w), 1655 (m), 1593 (vs), 1508 (vs), 1389 (m), 1331 (m), 1292 (m), 1234 (m), 1207 (s), 1099 (m), 833 (m), 540 (vs) (Figure A-118). PXRD (Previous Figure A-116) and TGA (Figure A-119) was recorded.

5.2.10 Impedance measurement

The impedance measurements were carried out using a pellet of the sample between the silver electrodes at room temperature (25 °C) and under wide frequency range 4Hz-5MHz using computer-interfaced HIOKI impedance analyser model IM3570. Impedance measurements were carried out with **CP1**, **CP2** and **CP1-BT**. **CP1-BT** was prepared by immersing the **CP1** crystals in benzotriazole for 2-3 days.

5.2.10.1 CP1-BT: Selected FTIR peaks (KBr, cm^{-1}): 2361(m), 2072 (s), 1670 (m), 1589 (vs), 1508 (vs), 1420 (m), 1331 (s), 1292 (m), 1207 (m), 1014 (m), 826 (m), 536 (vs) (Figure A-120) and PXRD (Figure A-121) of CP1-BT were recorded.

5.3 Results and discussion

The reaction of $Co(SCN)_2$ with N^1,N^3-di(pyridine-4-yl)isophthalamide (**L15b**) has resulted in the formation of **CP1**. Post-synthetic modification of **CP1**, wherein the transmetalation reaction of **CP1** with Cu(II) was performed, resulted in **CP2** (Scheme 5.2). Crystal structure analysis of **CP1** and **CP2** were done in order to study the impact of changing the metal center from Co(II) to Cu(II) on the CPs. Crystal data and structure refinements of **CP1** and **CP2** are summarized in Table 5.1. Although substantial changes were not observed in the overall network geometry of **CP1** and **CP2**, but the differences were mainly present in terms of coordination environment of the metal center and conformation of **L15b**.

Transmetalation reaction was monitored by atomic absorption spectroscopic analysis (AAS) and also by energy dispersive X-ray spectroscopy (EDX), wherein it was observed that more than 95% of the reaction was completed within 6 h duration (Figure 5.1a and Figure 5.1b). **CP1** and **CP2** were exploited as photocatalyst for degradation of organic dyes and kinetic studies of the photocatalysis were done. The presence of loops in the networks of **CP1** and **CP2**

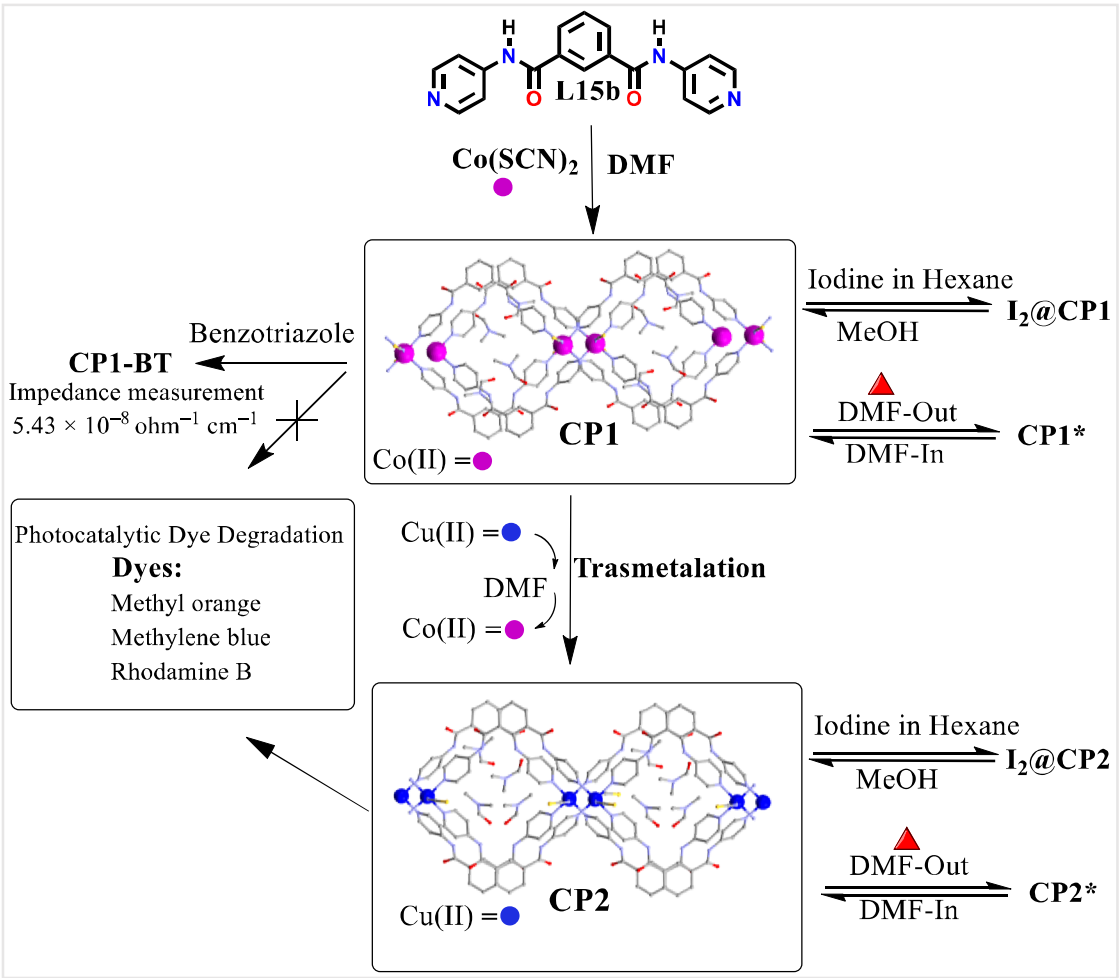

Scheme 5.2: Synthesis of **CP1** and **CP2**: Analysis of adsorption-desorption of iodine, solvochromism, photocatalytic dye degradation and impedance measurement

encouraged us to observe the properties associated with adsorption and desorption of iodine. Both **CP1** and **CP2** were able to incorporate iodine and resulted in iodine adsorbed CPs, **I_2@CP1** and **I_2@CP2** (Scheme 5.2). Further removing DMF from the networks of **CP1** and **CP2** resulted in **CP1*** and **CP2***, both of which showed significant color changes reflecting the changes in the coordination environment of metal centers on removing DMF (Scheme 5.2).

Table 5.1: Crystal structure data and refinement parameters for **CP1** and **CP2.**[a]

Parameters	**CP1**	**CP2**
Chemical formula	$C_{47}H_{49}CoN_{13}O_7S_2$	$C_{50}H_{56}CuN_{14}O_8S_2$
Formula Weight	1031.04	1108.74
Temperature (K)	296(2)	296(2)
Wavelength (Å)	0.71073	0.71073
Crystal system	Monoclinic	Monoclinic
Space group	*C2/c*	$P2_1/c$
a (Å)	25.248(8)	23.287(14)
b (Å)	14.575(4)	14.366(9)
c (Å)	17.180(5)	17.203(10)
α (°)	90	90
β (°)	118.501(7)	106.603(7)
γ (°)	90	90
Z	4	4
Volume ($Å^3$)	5556.0(3)	5515.0(6)
Density (g/cm^3)	1.233	1.335
μ (mm^{-1})	0.441	0.536
Theta range	1.84 ° to 25.07 °	0.91° to 25.04°
F(000)	2148	2316
Reflections collected	16260	53538
Independent reflection	4930	9719
Reflections with I >2σ(I)	3809	6546
R_{int}	0.0437	0.0691
Number of parameters	333	684
GO F on F^2	1.107	1.020
Final R_1[a]/wR_2[b] (I >2σ(I))	0.0721 / 0.2403	0.0493/ 0.1378
R_1[a]/wR_2[b] (all data)	0.0895 / 0.2587	0.0855/0.1704
Largest diff. peak and hole ($eÅ^{-3}$)	1.064 and -0.637	0.716 and -0.519

[a] $R_1 = \sum||F_o| - |F_c||/\sum|F_o|$. [b] $wR_2 = [\sum w(F_o^2 - F_c^2)^2/\sum w(F_o^2)^2]^{1/2}$, where $w = 1/[\sigma^2(F_o^2) + (aP)^2 + bP]$, $P = (F_o^2 + 2F_c^2)/3$.

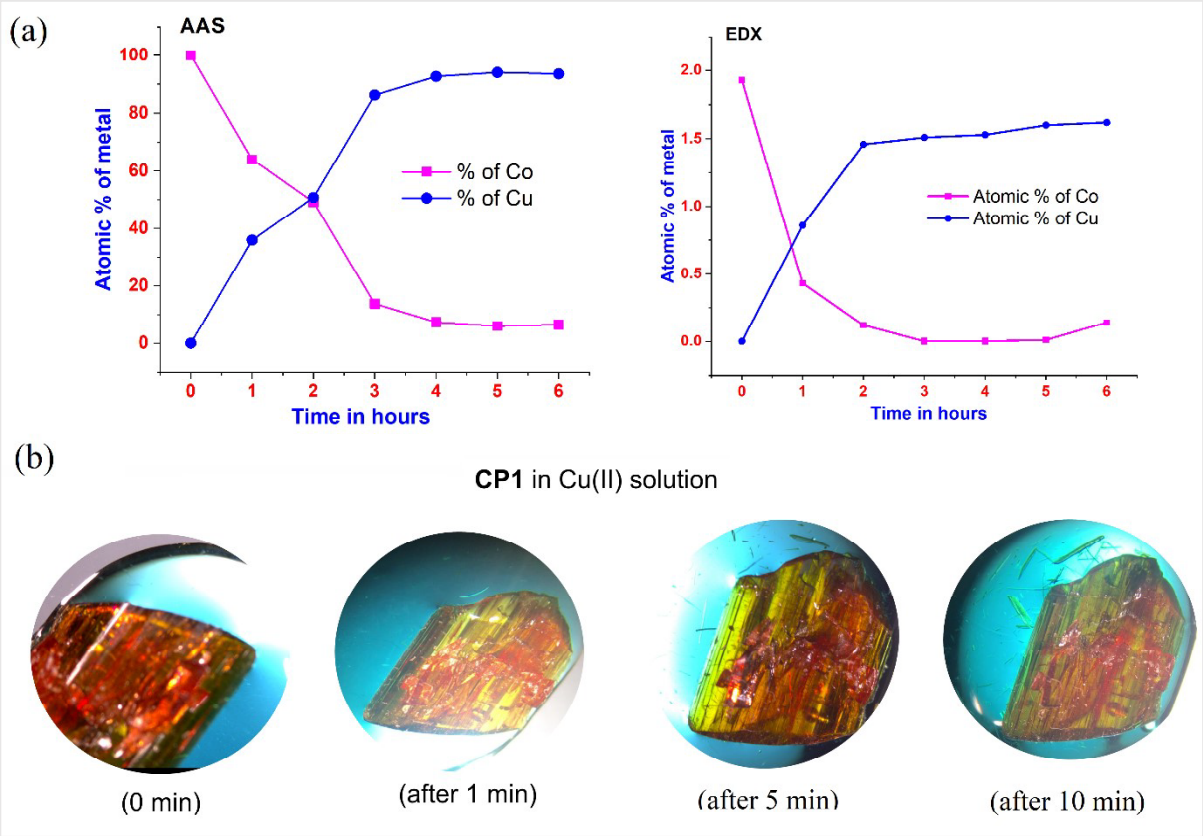

Figure 5.1: Transmetalation reaction of **CP1** with Cu(II): (a) Reaction kinetics monitored by EDX and (b) Images of single crystal to single crystal transformation of **CP1** to **CP2**

5.3.1 Crystal structure analysis of CP1

CP1 has crystallized into monoclinic *C*2/c space group in which each Co(II) center adopts a distorted octahedral geometry with two axial positions being occupied by the NCS^- anions, while **L15b** moieties satisfy the other four coordination sites. [Bond length: Co-N(**L15b**) 2.158 Å, 2.185 Å; Co-NCS 2.095 Å; Bond angle SCN-Co-N(**L15b**): 87.54°, 89.52°, 89.79°, 93.15°] (Figure 5.2). An ORTEP diagram of CP2 is shown in Figure A-122. In the crystal structure, three DMF molecules are found per Co(II). The ligand **L15b** has three aromatic moieties and two amide groups, which give an overall rigidity to the molecule. The possible structural modulations in **L15b** include the bond rotation which can only result in change in the interplanar angles between the aromatic planes and amidic planes. In order to analyse the geometry of **L15b** in **CP1**, molecule of **L15b** can be segregated into five different planes (Figure 5.3a). The

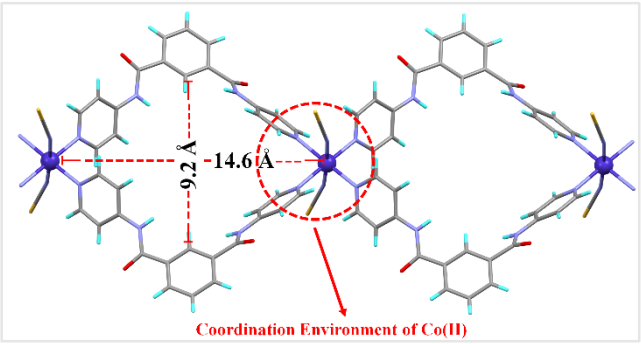

Figure 5.2: Illustration for crystal structure of CP1: (a) 1D looped chain in CP1

interplanar angles between these five planes are listed in Table 5.2. An important observation regarding the geometry of **L15b** in **CP1** is that the NH of both the amidic groups are pointing in the same direction and the interplanar angle between the two amidic planes (Plane D and Plane E) is 59.09°. This results in the attainment of a 'V' shaped geometry of **L15b** in **CP1**.

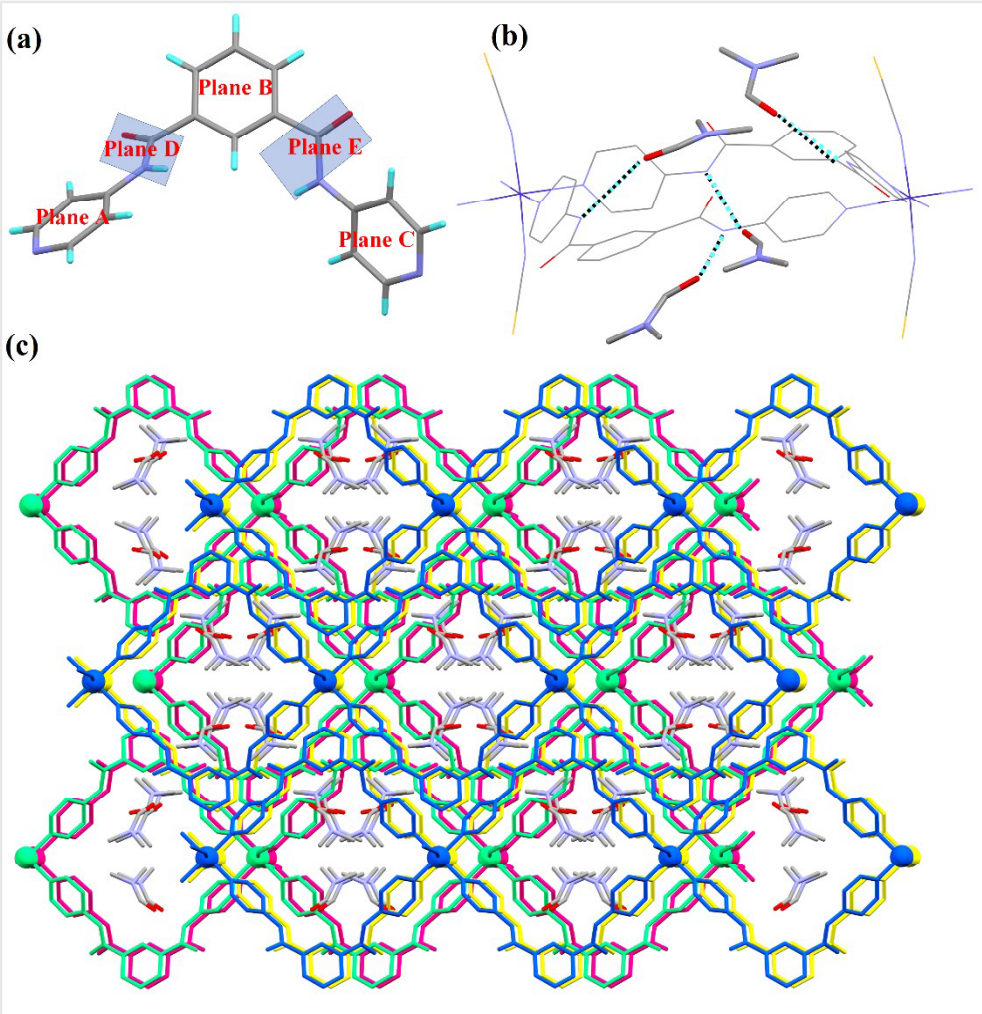

Figure 5.3: Illustration for crystal structure of **CP1**: (a) Geometry of **L15b** in **CP1**, (b) Hydrogen bond interaction of N-H groups in **CP1** with the DMF molecules (Hydrogen atoms are removed for clarity), (c) Offset packing of the 1D chains (Chains are shown in different colors for clarity)

Further the interplanar angle between the pyridyl plane (Plane A) and amidic plane (Plane D) is 4.21° while that between the pyridyl plane (Plane C) and amidic plane (Plane E) is 16.41°. The consequence of these interplanar angles between the pyridyl planes and amidic planes is the absence of self-complementary amide-to-amide hydrogen bonds between the adjacent **L15b** units in **CP1**, which may be due to the steric hindrance of the pyridyl groups. The 'V' shaped geometry of **L15b** in **CP1** and its further coordination to the Co(II) has resulted in the formation of 1D looped chain structure. The metal to metal distance within a loop is about 14.6 Å while the distance along the shorter axis of the loop is around 9.2 Å. The NH groups of **L15b**

are pointing towards the loops while the C=O of **L15b** is pointing away from the loops. The DMF molecules present in the network form hydrogen bond with the NH groups of **L15b**. For each loop in a chain of **L15b**, four DMF molecules form hydrogen bond with four NH moieties present in the loop, wherein two NH moieties are pointing upwards while two NH moieties are pointing downwards with respect to the plane of the loop involving the Co(II) centers (Figure 5.3b). The packing of 1D looped chains is in offset manner mainly due to the presence of NCS^- groups, which are coordinating to the Co(II) and pointing normal to the plane of the loops (Figure 5.3c).

5.3.2 Crystal structure analysis of CP2

The crystal structure analysis of **CP2** shows that it has crystalized in Monoclinic $P2_1/c$ space group and the asymmetric unit contains two **L15b** units, one Cu(II), two SCN^- and four DMF molecules. An ORTEP diagram of CP2 is shown in Figure A-123. The coordination sphere of Cu(II) has one SCN^- unit coordinated in the axial position along with four **L15b** units (Figure 5.4a). The sixth coordination site in Cu(II) has SCN^- ion but its distance is more than the bonding distance [Cu-N(**L15b**): 2.027 Å, 2.039 Å, 2.053 Å, 2.042 Å; Cu-NCS: 2.306 Å, 2.833 Å]. The presence of Cu(II) has resulted in an elongated geometry due to Jahn Teller distortion (Figure 5.4c). The distortion in the coordination sphere of the Cu(II) center has affected the **L15b** conformation as well and has incorporated more asymmetry in the structure of **CP2** compared to that of **CP1**. Unlike in **CP1**, **CP2** has two **15b** units in the asymmetric unit. The geometry of two types of **L15b** in **CP2** was analyzed more closely by segregating each **L15b** units into five planes and observing the interplanar angles between these planes (Figure 5.4b, Table 5.2).

Table 5.2: Orientations of aromatic planes of **L15b** in **CP1** & **CP2** [Planes are labelled in Figure 5.3a]

CP1		CP2			
		Type 1 (L15b)		Type 2 (L15b)	
Planes	Angles	Planes	Angles	Planes	Angles
Plane A and Plane B	47.56°	Plane P and Plane Q	50.73°	Plane U and Plane V	54.25°
Plane B and Plane C	39.13°	Plane Q and Plane R	44.71°	Plane V and Plane W	43.91°
Plane A and Plane C	67.31°	Plane P and Plane R	74.47°	Plane U and Plane W	74.48°
Plane A and Plane D	4.21°	Plane P and Plane S	21.55°	Plane U and Plane X	18.36°
Plane B and Plane D	44.06°	Plane Q and Plane S	30.33°	Plane V and Plane X	36.96°
Plane C and Plane D	66.17°	Plane R and Plane S	64.34°	Plane W and Plane X	66.29°
Plane A and Plane E	61.36°	Plane P and Plane T	74.60°	Plane U and Plane Y	65.31°
Plane B and Plane E	23.64°	Plane Q and Plane T	44.41°	Plane V and Plane Y	22.33°
Plane C and Plane E	16.41°	Plane R and Plane T	0.53°	Plane W and Plane Y	21.94°
Plane D and Plane E	59.09°	Plane S and Plane T	64.28°	Plane X and Plane Y	51.89°

Both the types of **L15b** in **CP2** attain 'V' shaped geometry. Self-complementary amide to amide hydrogen bond is absent in **CP2** and the NH groups of the amides are involved in hydrogen bond interaction with the DMF molecules (Figure 5.4d). Also, the interplanar angle between the amidic plane and the pyridyl plane (adjacent to the amide) is less (21.55°, 0.53°, 18.36° and 21.94°); which in turn will hinder the approach of amidic moiety of another **L15b** molecule to form hydrogen bond interactions due to steric reasons. The directionality of the hydrogen bond interaction is reflected in terms of conformational change of **L15b** and the shifting of one of the DMF molecules in loop of the network. Figure 5.3b and Figure 5.4d clearly illustrates the effect of conformational change of **L15b** in **CP1** and **CP2** on the positioning of the DMF molecules.

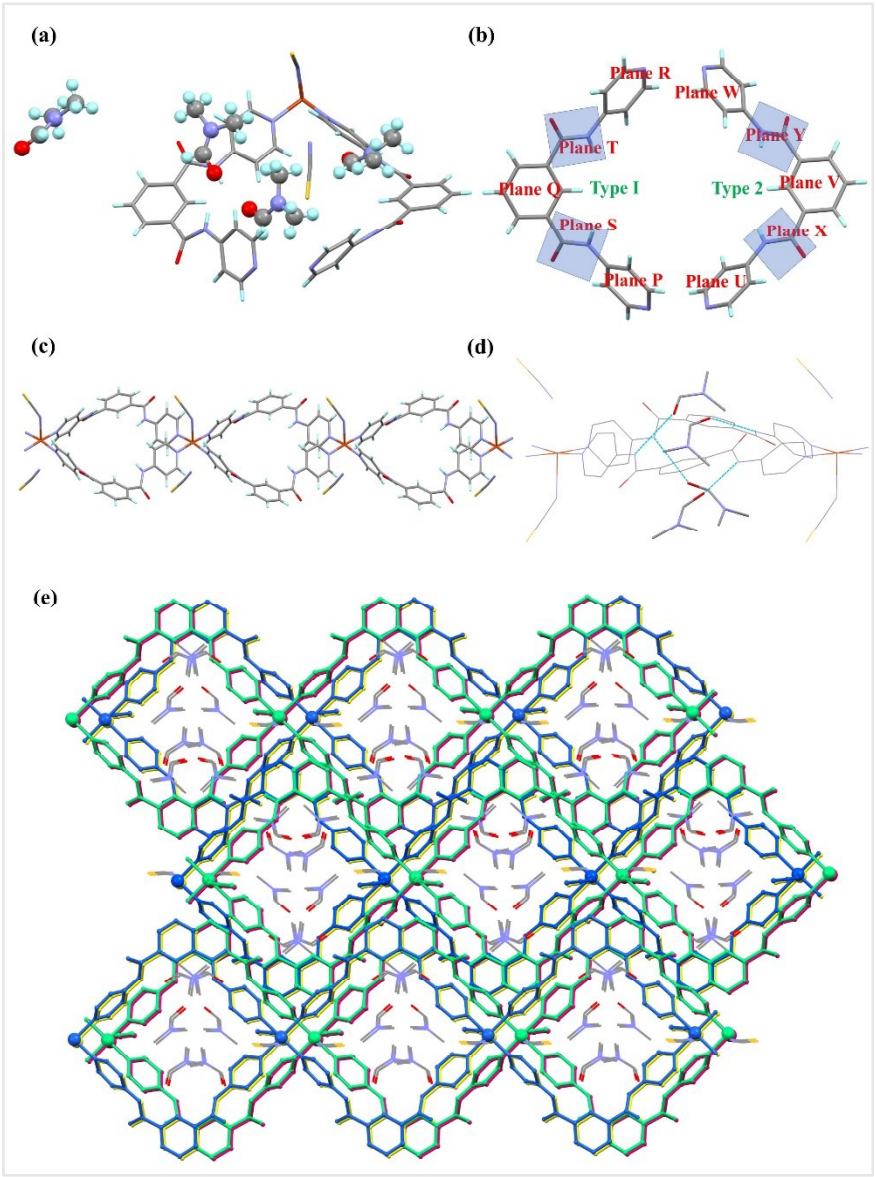

Figure 5.4: Illustration for crystal structure of **CP2**: (a) Asymmetric unit in **CP2**, (b) Geometry of two types of L**15b** in **CP2**, (c) 1D looped chain, (d) Hydrogen bond interaction of N-H groups in **CP2** with the DMF molecules (Hydrogen atoms are removed for clarity), (e) Offset packing of the 1D chains (Chains are shown in different colors for clarity)

5.3.3 Magnetic measurement of CP1

Magnetic direct-current (DC) susceptibility measurements in a 1 kOe magnetic field was performed as a function of temperature (from 1.9 K to 400 K) on pellets of the randomly oriented polycrystalline sample of **CP1**. The $\chi_m T$ (χ_m molar paramagnetic susceptibility) vs T plot of **CP1** is shown in Figure 5.5a at room temperature, the $\chi_m T$ product is 3.22 emu·K·mol^{-1} (μ_{eff} = 5.08 μB per Co (II) ion). This value is consistent with the expected value of 5.3 for Co^{2+} ions (S = 3/2 with large orbital contribution, so that g ≈ 2.5). The χ_m^{-1} vs T plot (Figure 5.5b) follows the Curie-Weiss law with Curie constant of 3.375 emu·K·mol^{-1}, is in well agreement with high spin Co(II) ions in an octahedral geometry. **CP1** has shown ferromagnetic interaction which is confirmed from the positive value of Weiss constant of 4.12.

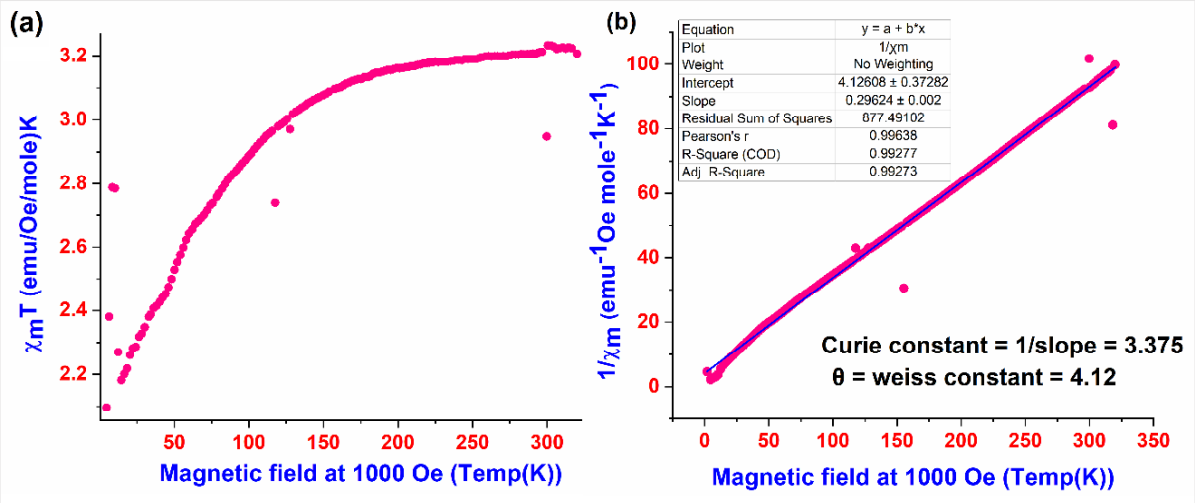

Figure 5.5: Temperature dependence molar magnetic susceptibility of **CP1** per formula unit: $\chi_m T$ vs T plot of **CP1** fits the Curie-Weiss law

5.3.4 Thermal gravimetric analysis of CP1 and CP2

For analyzing the thermal stability, 6.26 mg of **CP1** was taken and heated at a rate of 10 °C/min under N_2 atmosphere up to a temperature of 700 °C (Figure A-124). In the temperature range of 153 °C to 206 °C, one molecule of DMF was lost from **CP1** (Actual weight loss = 12.74%; Calculated weight loss for one DMF molecule = 13.23%) (Figure 5.6a). Another DMF molecule was lost in the temperature range of 219 °C to 277 °C. The degradation of **CP1** was observed at 313 °C to 446 °C with weight loss 49.78%, which corresponds to one molecule of **L15b** ligand (Calculated weight loss for one **L15b** molecule = 50.41%). The derivative plot, i.e., the first derivative of weight % w.r.t time (minute) vs. temperature (°C), of **CP1** and **CP1*** further clarifies the complete removal of the DMF molecules from **CP1***. TGA of **CP2** and **CP2*** shows similar behavior (Figures 5.6b and A-125).

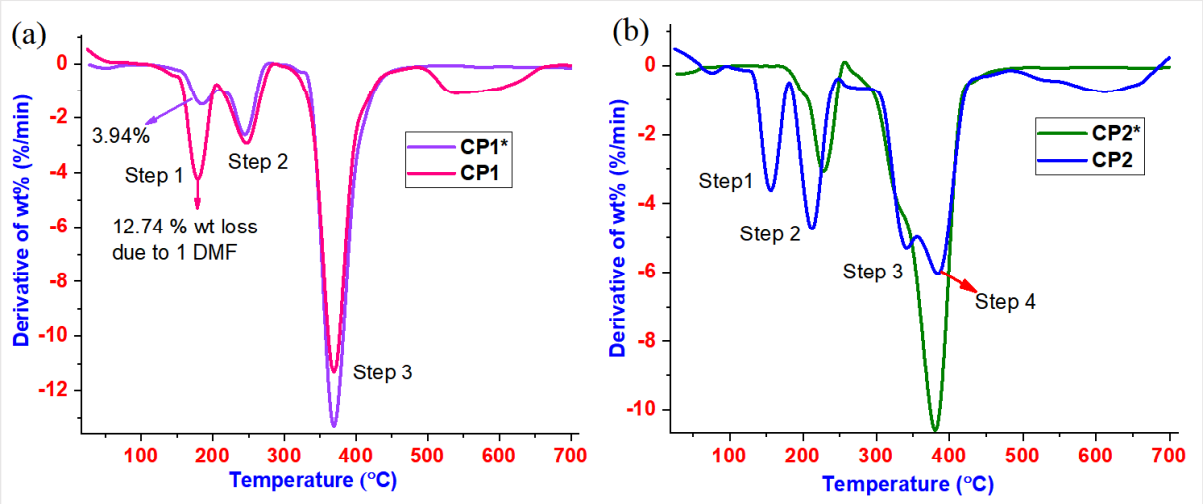

Figure 5.6: TGA derivative plot of weight% of (a) (**CP1** and **CP1*)** and (b) (**CP2** and **CP2***)

5.3.5 Solid state UV-visible absorption spectra studies

Solid-state UV-visible absorption spectra of **L15b**, **CP1** and **CP2** were recorded by mixing 5 mg of a compound (**L15b**/**CP1**/**CP2**) with 500 mg of $BaSO_4$. The UV-visible spectrum of **L15b** has two absorption maxima at 220 nm ($\pi \rightarrow \pi^*$) and 280 nm ($n \rightarrow \pi^*$) (Figure 5.7). The spectrum of **CP1** shows absorption maxima ~200 nm ($\pi \rightarrow \pi^*$) and ~281 nm ($n \rightarrow \pi^*$) along with a shoulder peak in the range 357-366 nm (due to DMF) and peaks corresponding to d-d transition at ~493 nm, a shoulder band at ~542 nm and another hump ~627 nm (Figure 5.8a).[76] If Co(II) is assumed to be of perfect octahedral geometry in **CP1** then the d-d transition can be labelled as ~493 nm ($^4T_{1g}$ (F) $\rightarrow$ $^4T_{1g}$(P)) and ~621 nm ($^4T_{1g}$(F) $\rightarrow$ $^4A_{2g}$(P)) in accordance with the Tanabe Sugano diagram for d^7 high spin system. The shoulder band ~542 nm indicates that the Co(II) has a distorted geometry resulting in lowering of the degeneracy of the ground electronic state. Along with natural distortion, Jahn Teller distortion is also evident from the fact that d^7 high spin state will have asymmetry in the t_{2g} orbital and is expected to show tetragonal compression. The tetragonal compression is also clear from the crystal structure, but the extent of distortion is not so pronounced in terms of bond lengths. The natural distortion in the bond angle i.e., deviation from 90°, is due to the steric factors.

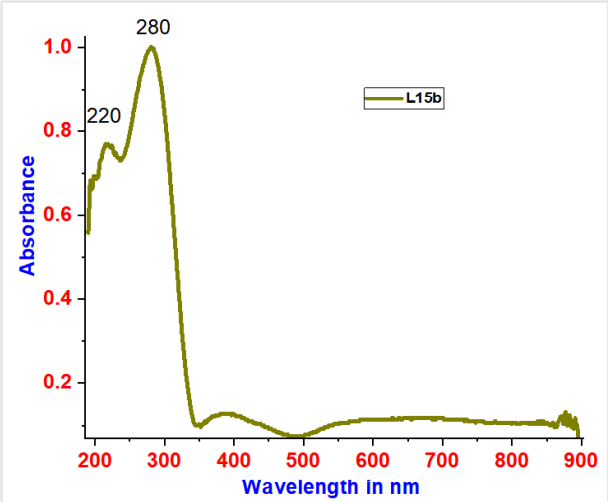

Figure 5.7: Solid state UV-visible spectrum of **L15b**

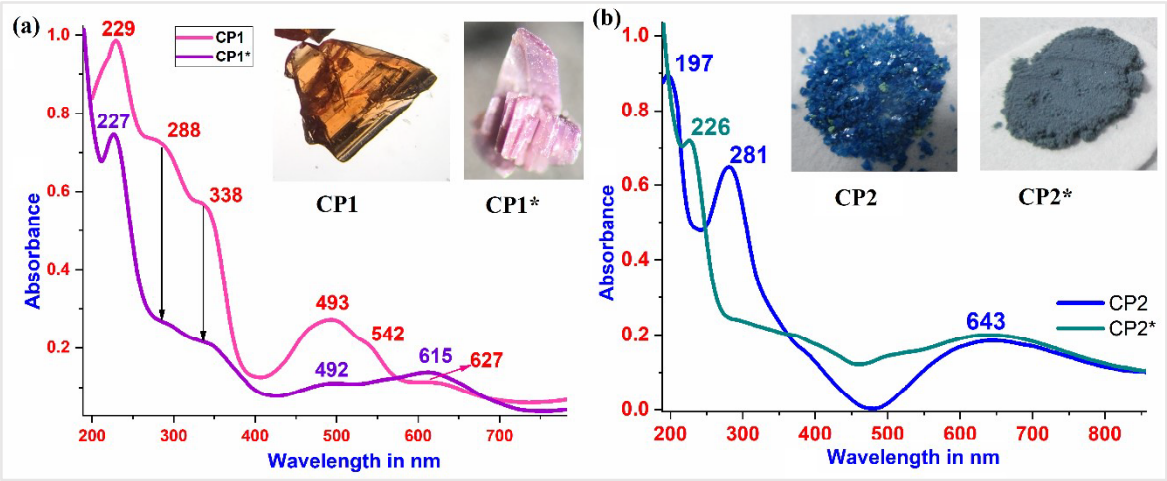

Figure 5.8: Solid state UV-visible spectra of (a) (**CP1** and **CP1***) and (b) (**CP2** and **CP2***)

CP1 has DMF guest molecules, which were removed by heating **CP1** crystals at a temperature of 120 °C under vacuum. The resultant crystals, **CP1***, showed a significant color change, which may be attributed to changes in the d-d transition (Figure 5.8a). The UV-visible spectrum of **CP1*** was recorded and a substantial decrease in the intensity of the peak in the range 357-366 nm was observed, which confirmed the removal of DMF. Further the peak due to d-d transition, ~493 nm ($^4T_{1g}(F) \rightarrow {}^4T_{1g}(P)$), also showed a reduction in intensity. In fact, the two d-d transition peaks, ~493 nm ($^4T_{1g}(F) \rightarrow {}^4T_{1g}(P)$) and ~627 nm ($^4T_{1g}(F) \rightarrow {}^4A_{2g}(P)$), were now observed to have almost similar intensity, with a quite less molar extinction coefficient. It may be inferred from the UV-visible spectrum that on removing the DMF, distortions along the Co(II) coordination sphere in **CP1*** has reduced, thereby validating the Laporte selection rule and consequently the reduction in molar extinction coefficient. The C=O of the DMF molecules in **CP1** were involved in hydrogen bond interactions with the N-H of **L15b**.

The UV-visible spectrum of **CP2** showed the peaks due to **L15b** (~200 nm and ~280 nm), a peak at around 320 nm for DMF and a peak at ~637 nm (due to d-d transition), which is comparatively more intense than that of **CP1** (Figure 5.8b). Natural distortion along with extreme Jahn Teller distortion (d^9 resulting in asymmetry in e_g orbital) is quite evident from the crystal structure analysis of **CP2**. In fact, the tetragonal elongation observed in **CP2** is so extreme that one of the SCN^- is beyond the bonding distance. Such distortions in **CP2** have direct effect on the intensity of the

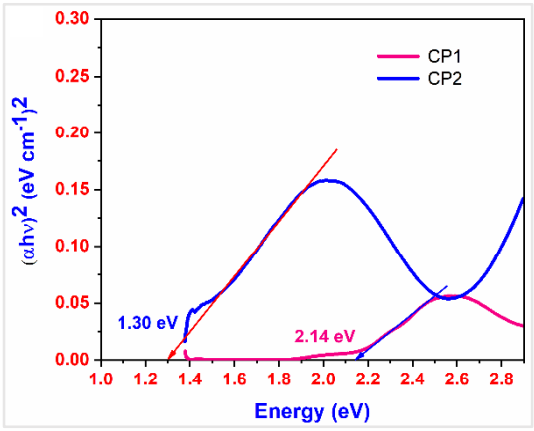

Figure 5.9: Tauc plot for band gap determination in **CP1** and **CP2**

d-d transition bands which showed an increased molar extinction coefficient. The band gap (E_g) was calculated by Tauc plot. The band gap of **CP1** was found to be 2.14 eV while that in **CP2** was calculated as 1.30 eV (Figure 5.9).

5.3.6 Photocatalytic degradation of organic dye molecules

The band gap of **CP1** (2.14 eV) and **CP2** (1.30 eV) showed that these CPs can act as potential photocatalyst. Photocatalytic activity of **CP1** and **CP2** toward the degradation of organic dyes was studied. The organic dye molecules, Methylene blue (MB), Rhodamine B (RB), Methyl orange (MO) and Malachite green (MG), were selected, which are considered as water pollutants. For photocatalytic activity, 20 mg of CP (**CP1** or **CP2**) is added to 20 mL of 10^{-5} M aqueous solution of an organic dye (MB, RB, MO or MG) and the mixture was kept under ordinary light. The UV visible absorption spectrum was recorded after every 30 min. time interval to analyze the decay of the dye (Figure A-126 to 128**)**. Similar dye degradation experiment was done under UV light as well (Figure 5.10). Figure 5.11a represents the percentage of dye degradation by **CP1** and **CP2** in mole %.

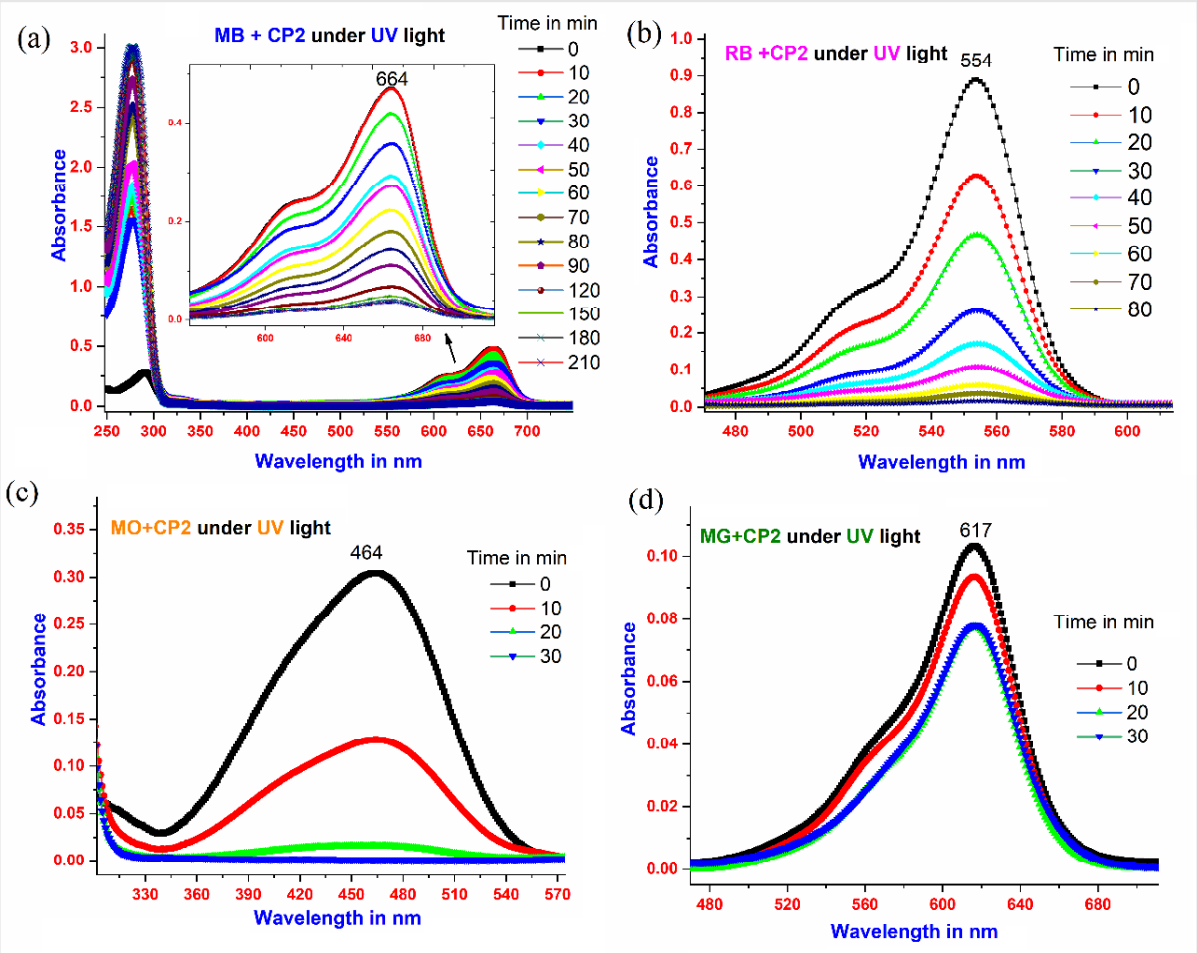

Figure 5.10: Dye degradation studies of **CP2** under UV light

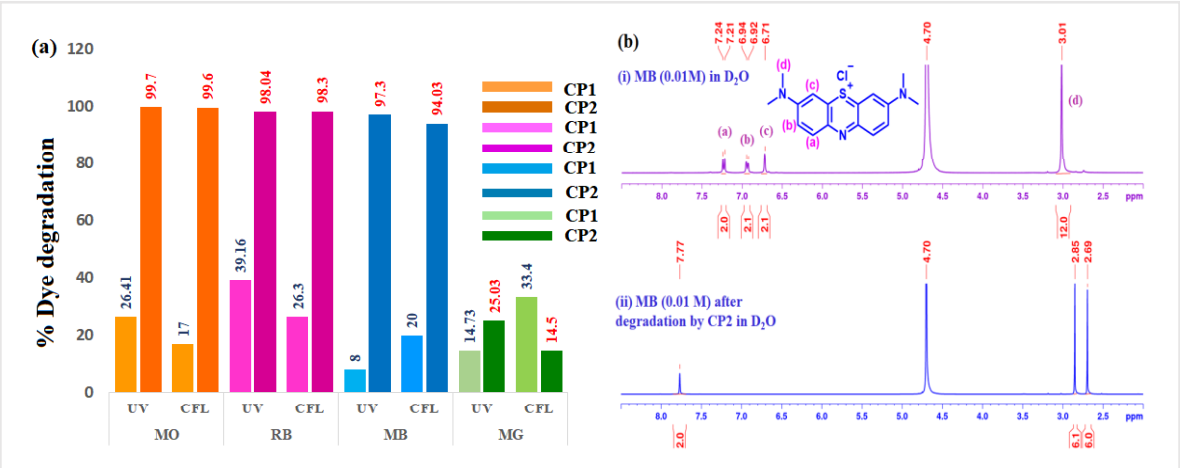

Figure 5.11: (a) % dye degradation by **CP1** and **CP2** under UV and CFL light (b) (i) ^{1}H-NMR spectrum of MB in D_2O and (ii) ^{1}H-NMR spectrum of MB after degradation by **CP2** under UV light

It was observed that **CP2** was more efficient in degrading MB, MO and RB under ordinary light (CFL) as well as UV light than that of **CP1**. The low band gap of **CP2** compared to that of **CP1** is reflected in terms of higher photocatalytic efficiency of **CP2** than that of **CP1**. The kinetics of MB degradation by **CP2** was found to follow 1st order kinetics and the slope plot *ln [MB]* vs. time, where [MB] is the molar concentration, was used to calculate the rate constant (3.14×10^{-4} s^{-1} for UV). Rate constants for the photodegradation of MO, RB and MG in presence of **CP2** are provided in appendix (Figure A-129). The mechanism of photocatalytic degradation of organic dyes by **CP1** and **CP2** is depicted in Figure 5.12.[77] The lower band gap in **CP2** resulted in creation of holes in the valence band, which are involved in the reduction of water molecules to hydroxyl radical (OH•) and the OH• further carry out the degradation of the dyes.

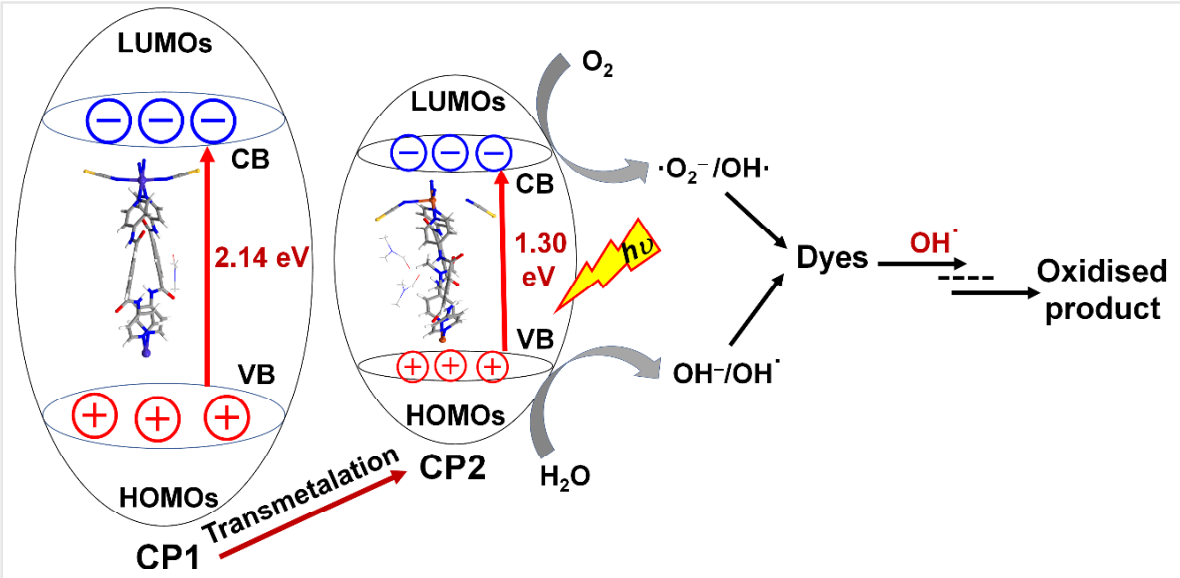

Figure 5.12: Schematic representation of charge transfer for photocatalytic degradation in CPs

In order to further verify the degradation of the dyes, MB degradation by **CP2** was also analyzed by NMR spectroscopy, where 0.01 M of MB dissolved in D_2O solvent and its ^{1}H-NMR spectrum was recorded. Then the solution was kept under UV light for one day after adding **CP2**. ^{1}H-NMR spectrum of the resultant solution showed a considerable change in the peak position of aromatic as well as in the aliphatic region (Figure 5A.11b). These changes indicate phenyl rings of MB molecule has been broken into small organic acids and inorganic ions.[78] The powder X-ray diffraction (PXRD) pattern has shown stability of the recovered samples after the photocatalysis (Figure A-130).

5.3.7 Adsorption-desorption of iodine in CP1 and CP2

Polar environment created due to the presence of DMF molecules near the loops of **CP1** and **CP2** has prompted us to study the adsorption and desorption of iodine from solution. To estimate the iodine adsorption, 5 mg of the CP (**CP1** or **CP2**) was dipped into a 10^{-4} M solution of iodine in hexane. In case of iodine adsorption by **CP1**, it was observed that after 7-9 hours, pink colored crystals of **CP1** were converted to dark brown without any change in the crystal morphology (Figure 5.13). The integrity of the host framework in the iodine adsorbed **CP1** was confirmed by PXRD studies (Figure A-131 to 132). The plot of $ln[I_2]$ with time showed that the I_2 adsorption in **CP1** and **CP2** follow the first order kinetics and the rate constants of **CP1** and **CP2** are calculated as 8.32×10^{-5} s^{-1} and 9.71×10^{-5} s^{-1}, respectively (Figure A-133). The amount of I_2 adsorbed by **CP1** and **CP2** were found to be 95.14 mole % and 95.66 mole %, respectively (Figure 5.14a and Figure 5.14c). Desorption of I_2 from **I_2@CP1** and **I_2@CP2** was done by soaking the compounds into methanol (Figure 5.14b and Figure 5.14d). The desorption process was monitored using UV-visible spectroscopy, wherein after 30 min. time interval, the absorbance of the solution was measured. For **I_2@CP1**, the absorbance at 359 nm increased with time, which indicated the release of iodine from the CP (Figure 5.14b). **I_2@CP2** has released I_2 at 265 nm within 8.5 hours and at 360 nm the negligible increase is observed (Figure 5.14d).

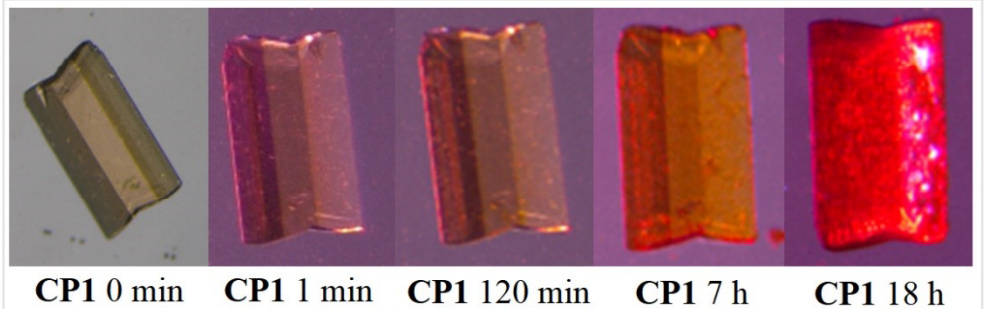

Figure 5.13: Microscope Images of Iodine adsorption in **CP1** over time

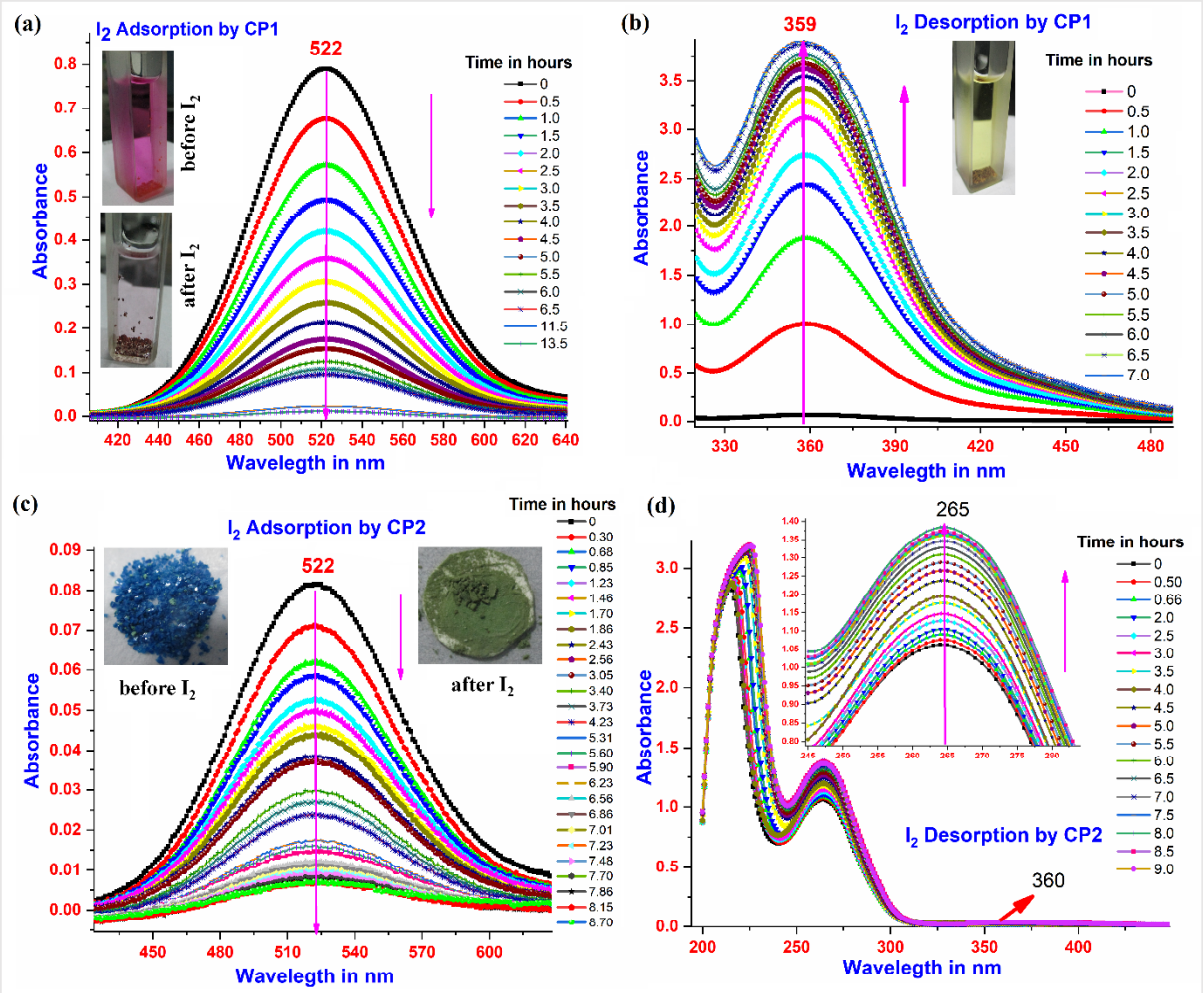

Figure 5.14: Adsorption of iodine by **CP1**, (b) Desorption of iodine from **CP1,** (c) Adsorption of iodine by **CP2**, (d) Desorption of iodine from **CP2**

5.3.8 Impedance measurement of CP1, CP2, and guest absorbed CP1

Impedance of **CP1**, **CP2** and benzotriazole incorporated **CP1**, **CP1-BT** (Scheme 5.2), were measured to study the electrical conductivities of the CPs due to capability of host guest interaction. Impedance, *Z*, is the total opposition a device or circuit offers to the flow of an alternate current at a given frequency. Figure 5.15a represents normalized impedance plot (Nyquist plot) of **CP1**, **CP2** and **CP1-BT**. The depressed semicircle arc in **CP1-BT** shows that it is a better conducting material than **CP1** and **CP2**. The conductivities of **CP1-BT**, **CP1** and **CP2** were calculated as 5.43×10^{-8} $ohm^{-1}cm^{-1}$, 3.54×10^{-9} $ohm^{-1}cm^{-1}$ and 3.33×10^{-9} $ohm^{-1}cm^{-1}$ respectively at the low-frequency region and it increases with increasing frequency up to 6.6×10^{-6} $ohm^{-1}cm^{-1}$, 4.43×10^{-6} ohm^{-1} cm^{-1}, and 6.0×10^{-6} $ohm^{-1}cm^{-1}$ respectively at 4.48×10^{6} Hz (Figure 5.15b). Initially, up to 10^{4} Hz, the conductivity of **CP1-BT** is independent of the frequency. In the modulus vs. frequency plot, more significant shift in peak position of **CP1-BT** was observed to the higher frequency region due to the motion of the

mobile charge (Figure 5.15c). Dielectric permittivity increases the sharply indicating ionic conduction mechanism is dominant at low frequency region for **CP1-BT** (Figure 5.15d). Impedance of **CP1** and **CP2** are polarized at high frequency region again proving that the accumulation of the ionic charges at the impedance interface. **CP1-BT** has shown more carrier transport to the free mobility of the ions due to the presence of benzotriazole as guest molecules.

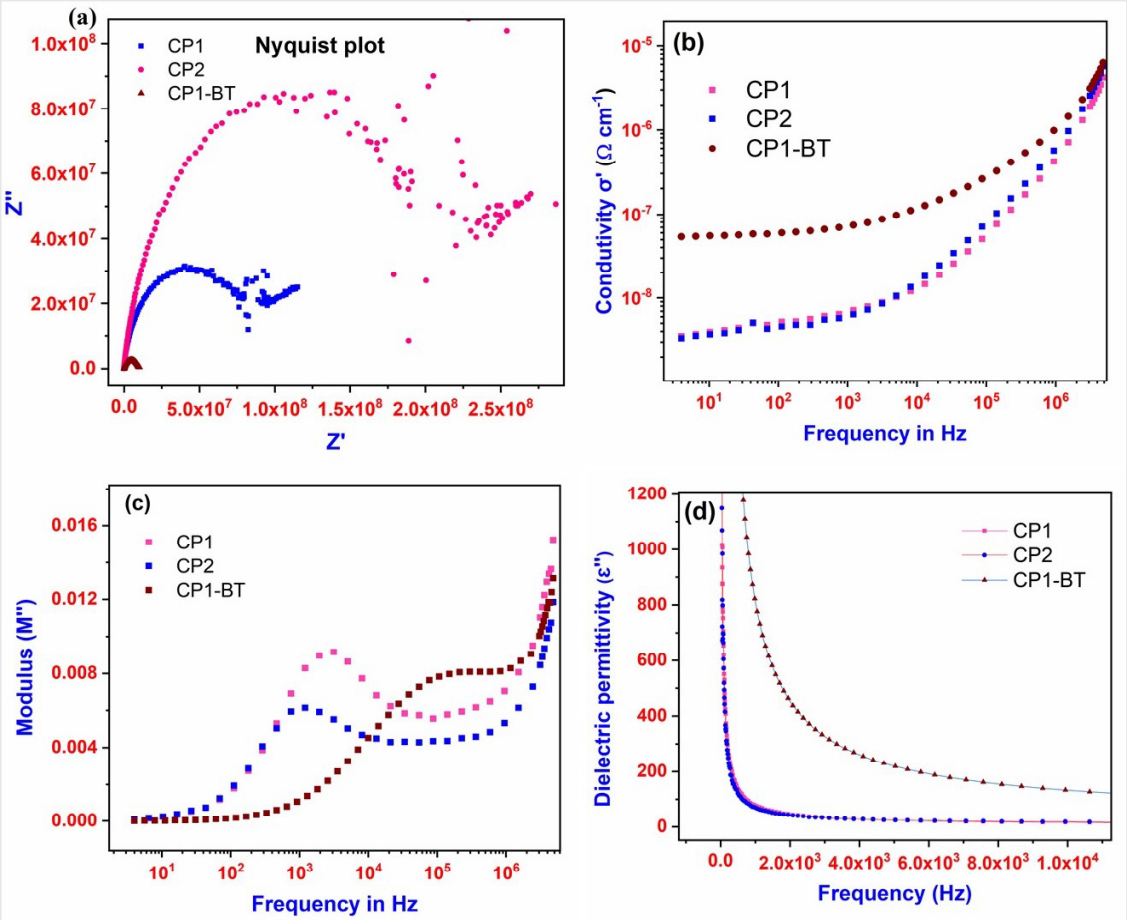

Figure 5.15: (a) Nyquist plot, (b) Conductivities vs. frequency plot, (c) Modulus vs. frequency plot, (d) Dielectric vs. frequency plot

5.4 Conclusion

N[1],*N*[3]-di(pyridine-4-yl)isophthalamide, an exo bidentate Bis(4-pyridyl)-diamide ligand having amide groups in the spacer, resulted in a one dimensional looped chain coordination polymer, **CP1** and trnasmetalation reaction on **CP1** with Cu(II) formed **CP2**, which is also 1D looped chain. A band gap of 2.41 eV and 1.30 eV, respectively, for **CP1**and **CP2** shows that these are potential photocatalysts thus photocatalytic dye degradation studies were done which showed a greater dye degradation efficiency of **CP2** compared to that of **CP1**. Presence of DMF as guest in both **CP1** and **CP2** has resulted in creating polar environment thereby facilitated the

adsorption of I_2 and the kinetics of I_2 adsorption showed a rate constant of 8.32×10^{-5} s^{-1} for CP1 and 9.71×10^{-5} s^{-1} for **CP2**. Impedance measurements showed a higher conductivity in the **CP1-BT**.

5.5 References

[1] (a) Rowsell J. L. C., Yaghi O. M., *Microporous Mesoporous Mater.,* **2004**, 73(1), 3-14; (b) He W.-W., Li S.-L., Lan Y.-Q., *Inorg. Chem. Front.,* **2018**, 5(2), 279-300.

[2] Dhakshinamoorthy A., Li Z., Garcia H., *Chem. Soc. Rev.,* **2018**, 47(22), 8134-8172.

[3] Kurmoo M., *Chem. Soc. Rev.,* **2009**, 38(5), 1353-1379.

[4] Lustig W. P., Mukherjee S., Rudd N. D., Desai A. V., Li J., Ghosh S. K., *Chem. Soc. Rev.,* **2017**, 46(11), 3242-3285.

[5] Bhardwaj S. K., Bhardwaj N., Kaur R., Mehta J., Sharma A. L., Kim K.-H., Deep A., *J. Mater. Chem. A,* **2018**, 6(31), 14992-15009.

[6] Della Rocca J., Liu D., Lin W., *Acc. Chem. Res.,* **2011**, 44(10), 957-968.

[7] Desiraju G. R., Parshall G. W., *Mater. Sci. Monogr.,* **1989**, 54.

[8] Stock N., Biswas S., *Chem. Rev.,* **2011**, 112(2), 933-969.

[9] (a) MacDonald J. C., Whitesides G. M., *Chem. Rev.,* **1994**, 94(8), 2383-2420; (b) Tong M.-L., Wu Y.-M., Ru J., Chen X.-M., Chang H.-C., Kitagawa S., *Inorg. Chem.,* **2002**, 41(19), 4846-4848.

[10] Sessler J. L., Gale P. A., Cho W.-S. *Anion receptor chemistry*: Royal Society of Chemistry; **2006**.

[11] Adarsh N., Kumar D. K., Dastidar P., *CrystEngComm,* **2009**, 11(5), 796-802.

[12] Adarsh N., Kumar D. K., Dastidar P., *Inorg. Chem. Commun.,* **2008**, 11(6), 636-642.

[13] (a) Adarsh N., Dastidar P., *Cryst. Growth Des.,* **2010**, 11(1), 328-336; (b) Adarsh N., Sahoo P., Dastidar P., *Cryst. Growth Des.,* **2010**, 10(11), 4976-4986.

[14] Adarsh N., Dastidar P., *Cryst. Growth Des.,* **2009**, 10(2), 483-487.

[15] Adarsh N., Grélard A., Dufourc E. J., Dastidar P., *Cryst. Growth Des.,* **2012**, 12(7), 3369-3373.

[16] Ghosh S., Mukherjee P. S., *Organometallics,* **2008**, 27(3), 316-319.

[17] Ghosh S., Gole B., Bar A. K., Mukherjee P. S., *Organometallics,* **2009**, 28(15), 4288-4296.

[18] Shanmugaraju S., Joshi S. A., Mukherjee P. S., *Inorg. Chem.,* **2011**, 50(22), 11736-11745.

[19] Bar A. K., Shanmugaraju S., Chi K.-W., Mukherjee P. S., *Dalton Trans.,* **2011**, 40(10), 2257-2267.

[20] Shanmugaraju S., Jadhav H., Patil Y. P., Mukherjee P. S., *Inorg. Chem.,* **2012**, 51(24), 13072-13074.

[21] Samanta D., Mukherjee P. S., *Dalton Trans.,* **2013**, 42(48), 16784-16795.

[22] (a) Shanmugaraju S., Bar A. K., Jadhav H., Moon D., Mukherjee P. S., *Dalton Trans.,* **2013**, 42(8), 2998-3008; (b) Shanmugaraju S., Bar A. K., Chi K.-W., Mukherjee P. S., *Organometallics,* **2010**, 29(13), 2971-2980.

[23] Gong Y., Zhou Y., Li J., Cao R., Qin J., Li J., *Dalton Trans.,* **2010**, 39(41), 9923-9928.

[24] Han L.-W., Gong Y., Lin Z.-J., Lü J., Cao R., *Dalton Trans.,* **2012**, 41(14), 4146-4152.

[25] Gong Y., Zhou Y.-C., Liu T.-F., Lü J., Proserpio D. M., Cao R., *Chem. Commun.,* **2011**, 47(21), 5982-5984.

[26] Gong Y., Li J., Qin J., Wu T., Cao R., Li J., *Cryst. Growth Des.,* **2011**, 11(5), 1662-1674.

[27] Gong Y., Li J., Jiang P.-G., Li Q.-F., Lin J.-H., *Dalton Trans.,* **2013**, 42(5), 1603-1611.

[28] Yue N. L., Eisler D. J., Jennings M. C., Puddephatt R. J., *Inorg. Chem.,* **2004**, 43(24), 7671-7681.

[29] Qin Z., Jennings M. C., Puddephatt R. J., *Chem. Commun.,* **2002**, 2002(4), 354-355.

[30] (a) Banerjee K., Roy S., Kotal M., Biradha K., *Cryst. Growth Des.,* **2015**, 15(11), 5604-5613; (b) Rajput L., Singha S., Biradha K., *Cryst. Growth Des.,* **2007**, 7(12), 2788-2795.

[31] Rajput L., Biradha K., *New J. Chem.,* **2010**, 34(11), 2415-2428.

[32] Rajput L., Biradha K., *CrystEngComm,* **2009**, 11(7), 1220-1222.

[33] Rajput L., Sarkar M., Biradha K., *J Chem Sci,* **2010**, 122(5), 707-720.

[34] Gong L. L., Feng X. F., Luo F., *Inorg. Chem.,* **2015**, 54(24), 11587-11589.

[35] Dang L.-L., Zhang X.-J., Zhang L., Li J.-Q., Luo F., Feng X.-F., *J. Coord. Chem.,* **2016**, 69(7), 1179-1187.

[36] Luo F., Sun G.-M., Zheng A.-m., Lian S.-x., Liu Y.-l., Feng X. F., Chu Y.-y., *Dalton Trans.,* **2012**, 41(43), 13280-13283.

[37] Sun G.-m., Huang H.-x., Tian X.-z., Song Y.-m., Zhu Y., Yuan Z.-j., Xu W.-y., Luo M.-b., Liu S.-j., Feng X.-f., *CrystEngComm,* **2012**, 14(19), 6182-6189.

[38] Yuan Z.-Z., Luo F., Song Y.-m., Sun G.-m., Tian X.-z., Huang H.-x., Zhu Y., Feng X.-f., Luo M.-b., Liu S.-j., *Dalton Trans.,* **2012**, 41(41), 12670-12673.

[39] (a) Lalonde M., Bury W., Karagiaridi O., Brown Z., Hupp J. T., Farha O. K., *J. Mater. Chem. A,* **2013**, 1(18), 5453-5468; (b) Evans J. D., Sumby C. J., Doonan C. J., *Chem. Soc. Rev.,* **2014**, 43(16), 5933-5951.

[40] Das S., Kim H., Kim K., *J. Am. Chem. Soc.,* **2009**, 131(11), 3814-3815.

[41] Kim Y., Das S., Bhattacharya S., Hong S., Kim M. G., Yoon M., Natarajan S., Kim K., *Chemistry–A European Journal,* **2012**, 18(52), 16642-16648.

[42] Tian J., Saraf L. V., Schwenzer B., Taylor S. M., Brechin E. K., Liu J., Dalgarno S. J., Thallapally P. K., *J. Am. Chem. Soc.,* **2012**, 134(23), 9581-9584.

[43] Pal T. K., De D., Neogi S., Pachfule P., Senthilkumar S., Xu Q., Bharadwaj P. K., *Chem. Eur. J.,* **2015**, 21(52), 19064-19070.

[44] Liu T.-F., Zou L., Feng D., Chen Y.-P., Fordham S., Wang X., Liu Y., Zhou H.-C., *J. Am. Chem. Soc.,* **2014**, 136(22), 7813-7816.

[45] Gupta M., De D., Pal S., Pal T. K., Tomar K., *Dalton Trans.,* **2017**, 46(23), 7619-7627.

[46] Bommakanti S., Venkataramudu U., Das S. K., *Cryst. Growth Des.,* **2018**, 19(2), 1155-1166.

[47] Suman K., Baig F., Gupta V. K., Mandal S., Sarkar M., *RSC Adv.,* **2014**, 4(69), 36451-36457.

[48] Khan S., Malik A., *Environmental Deterioration and Human Health: Natural and anthropogenic determinants*. Springer Netherlands; **2014**:55-71.

[49] (a) Zhang F., Li Y.-H., Li J.-Y., Tang Z.-R., Xu Y.-J., *Environ. Pollut.,* **2019**, 253, 365-376; (b) Zhang N., Yang M.-Q., Liu S., Sun Y., Xu Y.-J., *Chem. Rev.,* **2015**, 115(18), 10307-10377.

[50] (a) Martha S., Chandra Sahoo P., Parida K. M., *RSC Adv.,* **2015**, 5(76), 61535-61553; (b) Khan M. M., Adil S. F., Al-Mayouf A., *J. Saudi Chem. Soc.,* **2015**, 19(5), 462-464.

[51] Gautam S., Agrawal H., Thakur M., Akbari A., Sharda H., Kaur R., Amini M., *J. Environ. Chem. Eng.,* **2020**, 8(3), 103726.

[52] Zhang L. L., Xiong Z., Zhao X. S., *ACS Nano,* **2010**, 4(11), 7030-7036.

[53] Gu L., Wang J., Cheng H., Zhao Y., Liu L., Han X., *ACS Appl. Mater. Interfaces,* **2013**, 5(8), 3085-3093.

[54] Yuan L., Yang M.-Q., Xu Y.-J., *Nanoscale,* **2014**, 6(12), 6335-6345.

[55] Tang Z.-R., Zhang Y., Zhang N., Xu Y.-J., *Nanoscale,* **2015**, 7(16), 7030-7034.

[56] Weng B., Qi M.-Y., Han C., Tang Z.-R., Xu Y.-J., *ACS Catal.,* **2019**, 9(5), 4642-4687.

[57] Dhaka S., Kumar R., Deep A., Kurade M. B., Ji S.-W., Jeon B.-H., *Coord. Chem. Rev.,* **2019**, 380, 330-352.

[58] Wu Z., Yuan X., Zhang J., Wang H., Jiang L., Zeng G., *ChemCatChem,* **2017**, 9(1), 41-64.

[59] Liu L., Ding J., Huang C., Li M., Hou H., Fan Y., *Cryst. Growth Des.,* **2014**, 14(6), 3035-3043.

[60] Bala S., Bhattacharya S., Goswami A., Adhikary A., Konar S., Mondal R., *Cryst. Growth Des.,* **2014**, 14(12), 6391-6398.

[61] Mahata P., Madras G., Natarajan S., *J. Phys. Chem. B,* **2006**, 110(28), 13759-13768.

[62] Dong J.-P., Shi Z.-Z., Li B., Wang L.-Y., *Dalton Trans.,* **2019**, 48(47), 17626-17632.

[63] Liu C.-X., Zhang W.-H., Wang N., Guo P., Muhler M., Wang Y., Lin S., Chen Z., Yang G., *Chem. Eur. J.,* **2018**, 24(63), 16804-16813.

[64] Bedia J., Muelas-Ramos V., Peñas-Garzón M., Gómez-Avilés A., Rodríguez J. J., Belver C., *Catalysts,* **2019**, 9(1).

[65] Navarathna C. M., Dewage N. B., Karunanayake A. G., Farmer E. L., Perez F., Hassan E. B., MIsna T. E., Pittman C. U., *J. Inorg. Organomet. Polym. Mater.,* **2020**, 30(1), 214-229.

[66] Wang Q., Gao Q., Al-Enizi A. M., Nafady A., Ma S., *Inorg. Chem. Front.,* **2020**, 7(2), 300-339.

[67] Givaja G., Amo-Ochoa P., Gómez-García C. J., Zamora F., *Chem. Soc. Rev.,* **2012**, 41(1), 115-147.

[68] Bureekaew S., Horike S., Higuchi M., Mizuno M., Kawamura T., Tanaka D., Yanai N., Kitagawa S., *Materials For Sustainable Energy: A Collection of Peer-Reviewed Research and Review Articles from Nature Publishing Group*. World Scientific; **2011**:232-237.

[69] Fuma Y., Ebihara M., Kutsumizu S., Kawamura T., *J. Am. Chem. Soc.,* **2004**, 126(39), 12238-12239.

[70] You Y.-W., Xue C., Tian Z.-F., Liu S.-X., Ren X.-M., *Dalton Trans.,* **2016**, 45(18), 7893-7899.

[71] Takaishi S., Hosoda M., Kajiwara T., Miyasaka H., Yamashita M., Nakanishi Y., Kitagawa Y., Yamaguchi K., Kobayashi A., Kitagawa H., *Inorg. Chem.,* **2008**, 48(19), 9048-9050.

[72] Himoto K., Suzuki S., Okubo T., Maekawa M., Kuroda-Sowa T., *New J. Chem.,* **2018**, 42(6), 3995-3998.

[73] Dey C., Kundu T., Banerjee R., *Chem. Commun.,* **2012**, 48(2), 266-268.

[74] *Bruker, APEX2, V2008. 6, SADABS V2008/1, SAINT V7. 60A, SHELXTL V6. 14,* ***2008.***

[75] Sheldrick G. M., *Acta Crystallogr. Sect. A: Found. Crystallogr.,* **2008**, 64(1), 112-122.

[76] Lever A. B. P. *Inorganic electronic spectroscopy*. Amsterdam; New York: Elsevier Pub. Co.; **1968**.

[77] (a) Wen L., Zhou L., Zhang B., Meng X., Qu H., Li D., *J. Mater. Chem.,* **2012**, 22(42), 22603-22609; (b) Roy M., Adhikary A., Mondal A. K., Mondal R., *ACS Omega,* **2018**, 3(11), 15315-15324; (c) Wang C.-C., Li J.-R., Lv X.-L., Zhang Y.-Q., Guo G., *Energy Environ. Sci.,* **2014**, 7(9), 2831-2867.

[78] Ibrahim A. M., Al-Ashqar S. M., *Spectrochim. Acta, Part A,* **2012**, 92, 238-244.